

Supporting Information:

A new approach to preparing porous carbons with controllable pore structure and morphology

Yi Gu,^a Zhigang Xiong,^a Wael Al Abdulla,^b Guohua Chen,^c and X. S. Zhao^{*a}

^a School of Chemical Engineering, The University of Queensland, St Lucia, Brisbane, QLD 4072, Australia.

E-mail: george.zhao@uq.edu.au; Fax: +61-733654199; Tel: +61-733469997

^b Australian Institute for Bioengineering and nanotechnology (AIBN), The University of Queensland, St Lucia, Brisbane, QLD 4072, Australia

^c Centre for Green Products and Processing Technologies, Guangzhou HKUST Fok Ying Tung Research Institute, Guangzhou 511458, China

Experimental

Sample preparation

1,2,3,4-butanetetracarboxylic acid (BTCA), ethylenediamine (ED), pyromellitic dianhydride (PMDA), 3,4,9,10-pyrenetetracarboxylic dianhydride (PTCDA), and *p*-phenylenediamine (PPD) were purchased from Alfa-Aesar. Other chemicals used in this work were from Sigma-Aldrich. All chemicals were used as received.

A two-step method was used to prepare the porous carbon samples. Step-1 was to make a pre-formed carbonaceous network by mixing polycarboxylic acid/anhydride, diamine, and metal salt at room temperature. In the preparation of sample P-BTCA/ED/Zn, 10 mmol BTCA dissolved in 120 mL methanol and 20 mmol ED dissolved in 80 mL methanol were mixed under vigorous stirring. Very shortly, solid precipitates formed. The precipitates were then filtered out and added into 100 mL methanol containing 5 mmol Zn(NO₃)₂·6H₂O. The mixture was stirred at room temperature till the methanol fully evaporated to leave behind a carbonaceous network, which is designated as P-BTCA/ED/Zn. In the preparation of sample P-PMDA/PPD/Fe, 10 mmol PMDA dissolved in 120 mL methanol was mixed with 20 mmol PPD dissolved in 80 mL methanol under stirring. Then, 10 mL deionized (DI) water was added. After 30 min, 100 mL methanol containing 5 mmol Fe(NO₃)₃·9H₂O was added. The mixture was stirred at room temperature till the solvents fully evaporated to end up with a carbonaceous network (designated as P-PMDA/PPD/Fe). In the preparation of sample P-PTCDA/PPD/Fe, 10 mmol PTCDA was pre-dissolved in 100 mL DI water to allow hydrolysis for 2 h at room temperature. After that, 20 mmol PPD dissolved in 80 mL methanol was added under stirring. After 30 min, 100 mL methanol containing 5 mmol Fe(NO₃)₃·9H₂O was added. The mixture was stirred at room temperature till the solvents fully evaporated to end up with a carbonaceous network (designated as P-PTCDA/PPD/Fe).

Step-2 was to pyrolyze the carbonaceous networks obtained in Step-1, and remove the inorganic residues. All samples were heated in a tube furnace at the following temperatures for 3 h with a heating rate of 5 °C min⁻¹ under Ar flow (30 mL min⁻¹): P-BTCA/ED/Zn at 700 °C, P-PMDA/PPD/Fe at 800 °C and P-PTCDA/PPD/Fe at 900 °C. The pyrolysis temperature was chosen differently due to the difference of the carbon precursors. The pyrolysis products thus obtained were acid treated with HCl (1 M), followed by washing with DI water, and finally dried in a

vacuum oven at 120 °C overnight. The final products are designated as C-BTCA/ED, C-PMDA/PPD, and C-PTCDA/PPD, correspondingly.

Characterization

X-ray diffraction (XRD) patterns were recorded on a Bruker D8 Advance X-ray diffractometer using nickel-filtered Cu-K α radiation. N₂ physisorption measurement was performed at 77 K on a Micromeritics TriStar II 3020. All samples were degassed at 120 °C for 12 h before measurement. The SSA was determined by using the Brunauer-Emmett-Teller (BET) method. Then total pore volume was estimated from the nitrogen volume adsorbed at the relative pressures equal to 0.99. The micropore volume was determined by applying a t-plot analysis (Harkins and Jura thickness equation). The micropore size distribution was determined by using the density functional theory (DFT) model and the N₂ adsorption data, assuming a slit pore geometry.¹ The mesopore size distribution was determined by using the Kruk-Jaroniec-Sayari method applied to N₂ adsorption branches.² The morphology of the samples was observed on JEOL 7001F field-emission scanning electron microscopy (FESEM) at an acceleration voltage of 10 kV. The high-resolution transmission electron microscopy (HRTEM) was recorded on a JEOL 2100 microscope operated at 200 kV. X-ray photoelectron spectroscopy (XPS) spectra were acquired on a Kratos Axis ULTRA X-ray photoelectron spectrometer with a 165 mm hemispherical electron energy analyser and a monochromatic Al K α (1486.6 eV) radiation at 225 W (15 kV, 15 mA). Raman spectra were recorded on a Thermo-Fischer Almega dispersive Raman instrument. The instrument was fitted with both 633 and 785 nm lasers. Powder samples were measured at 25 °C using the microscope accessory with a 10 \times or 50 \times aperture between wave numbers 200-4000 cm⁻¹ with at least 132 scans. Fourier transform infrared (FTIR) spectra were recorded on a Perkin Elmer Spectrum 100 spectrophotometer. UV-vis absorption spectra were obtained using a Shimadzu UV-2600 spectrophotometer at room temperature.

Electrochemical measurements

The electrochemical measurements were performed on an Autolab PGSTAT302N workstation with 1 M H₂SO₄ aqueous electrolyte in a symmetric cell configuration. Each electrode was prepared by mixing a dry sample (95 wt%) with polytetrafluoroethylene (5 wt%), and pressed on a stainless steel mesh as the current collector. The electrodes were dried at 150 °C for 2 h. The mass loading of the electrode material was \sim 1.5 mg cm⁻². Two electrodes with a very close mass were assembled in a sandwich-type cell with active sides facing each other, and a Whatman filter paper was applied as the separator. The electrolyte was introduced by vacuum impregnation, and the cell was immersed in the electrolyte 24 h before measurement. The capacitive performance of samples was characterized by using the cyclic voltammetry (CV), galvanostatic charge-discharge (GCD) and electrochemical impedance spectroscopy (EIS) techniques. The specific gravimetric capacitance of a single electrode, C (in F g⁻¹), was obtained from the galvanostatic discharge curve according to $C = 4 \times I \times \Delta t / (m \times \Delta V)$,³ where I is the current load (in A), Δt is the discharge time (in s), ΔV is the potential change during discharge (in V), and m is the total mass loading on both electrodes (in g). By multiplying a factor 4, the specific capacitance measured in a two-electrode configuration can be transferred to an equivalent value estimated using a three-electrode configuration.³ This is solely for the purpose of comparing with literature data.

Table S1 Summary of textural and chemical properties of samples

Sample	$S_{BET}/m^2\ g^{-1}$	$V_{total}^a/cm^3\ g^{-1}$	$V_{micro}^b/cm^3\ g^{-1}$	$V_{meso}^c/cm^3\ g^{-1}$	C ^d at. %	N ^d at. %	O ^d at. %	I_D/I_G^e
C-BTCA/ED	455	0.255	0.200	0.055	87.56	7.94	4.50	1.19
C-PMDA/PPD	439	0.477	0.037	0.440	96.93	0.80	2.27	1.44
C-PTCDA/PPD	311	0.242	0.095	0.147	97.31	0.65	2.04	1.16

^a Total pore volume at P/Po \sim 0.99. ^b Micropore volume calculated by the t-plot technique. ^c Mesopore volume obtained by the difference between total pore volume and micropore volume. ^d Elemental compositions determined from XPS data. ^e Ratios of peak intensities calculated from Raman spectroscopy.

The CV and GCD data of electrode C-BTCA/ED are shown in Figs. S1a and S1b, respectively. The strong distortion of the CV curves of electrode C-BTCA/ED was due to low electric conductivity of the electrode and poor penetration rate of the electrolyte ions. The small micropores (1.09 nm in diameter) of this electrode posed a strong diffusion resistance towards the electrolyte ions, while the low carbonization degree of sample C-BTCA/ED caused the poor electronic conductivity. The obvious curvatures observed from the GCD curves at small charge-discharge current densities (i.e., 0.1 and 0.2 A g⁻¹) indicated the total capacitance came from both pseudocapacitance and electric double-layer (EDL) capacitance. The pseudocapacitance mainly originated from the N- and O-containing groups on the sample (see Table S1, ESI). Because the pseudocapacitance mechanism involves redox reactions, which are relatively slower than the formation rate of EDL, the pseudocapacitance became more obvious at a small charge-discharge current density. By increasing the current density, the EDL capacitance gradually dominated.

Figs. S1c and S1d illustrate the CV and GCD curves of electrode C-PTCDA/PPD, respectively. Due to its porous nanosheet structure, electrode C-PTCDA/PPD revealed a better rate performance than electrode C-BTCA/ED. An ideal CV curve can be seen at scan rates up to 100 mV s⁻¹. The quasi-rectangular GCD curves at all charge-discharge current densities implied that the EDL mechanism was the dominant charge storage mechanism in this electrode, agreeing well with the fact that this sample had a very low content of heteroatoms.

Fig. S1e compares the evolution of discharge current density versus scan rate of electrodes C-BTCA/ED, C-PMDA/PPD and C-PTCDA/PPD. As discussed in the main text, C-PMDA/PPD has a nearly linear dependence with a slight deviation at the scan rate of 500 mV s⁻¹. However, the linear dependence of electrode C-PTCDA/PPD began to deviate at the scan rate of 200 mV s⁻¹, and becoming more obvious at 500 mV s⁻¹. The deviation was very obvious on electrode C-BTCA/ED, of which the current evolution was hardly proportional to the scan rate in the small scan rate region below 50 mV s⁻¹. The poor rate performance of C-PTCDA/PPD and C-BTCA/ED was due to their lack of mesopores.

The specific capacitance as a function of current density of the three samples is shown in Fig. S1f. Electrode C-PMDA/PPD showed the best specific capacitance retention of 67% when the current density was increased from 0.1 to 20 A g⁻¹. The good power density was attributed to its hierarchical pore structure with both mesopores and micropores. Electrode C-PTCDA/PPD possessing a hierarchical pore structure with an open nanosheet morphology also exhibited a good specific capacitance of 141 F g⁻¹ at the current density of 0.1 A g⁻¹, and a reasonable capacitance retention of 50% when current density was increased from 0.1 to 20 A g⁻¹. The poorer capacitance retention of electrode C-PTCDA/PPD was due to its lower SSA and porosity in comparison with electrode C-PMDA/PPD. Electrode C-BTCA/ED showed a very interesting behaviour: it displayed a very high specific capacitance (238 F g⁻¹) at the current density of 0.1 A g⁻¹ and a nearly zero capacitance at the current density of 2 A g⁻¹. The rapid decay of specific capacitance with increasing current density was attributed to its micropore structure,

which posed a strong diffusion resistance towards electrolyte ions when charging-discharging at high current densities.

Fig. S1g shows the Nyquist plots of the three electrodes. Electrodes C-PMDA/PPD and C-PTCDA/PPD exhibited almost a vertical line in the low frequency region, implying that both electrode store energy according to the EDL mechanism. At the high frequency region, both electrodes showed a small semicircle, indicating a small ESR (1.38 and 1.35 Ω for C-PMDA/PPD and C-PTCDA/PPD, respectively), as well as a small charge transfer resistance (0.5 and 0.4 Ω for C-PMDA/PPD and C-PTCDA/PPD, respectively). Whilst on the C-BTCA/ED electrode, an obvious semicircle was seen at the high frequency region with an ESR of 1.7 Ω and a charge transfer resistance of $\sim 23 \Omega$. A typical Warburg region followed the semicircle indicated its capacitance was limited by the electrolyte ion diffusion. The poor impedance response of C-BTCA/ED was a result of its small pores and poor graphitization degree.

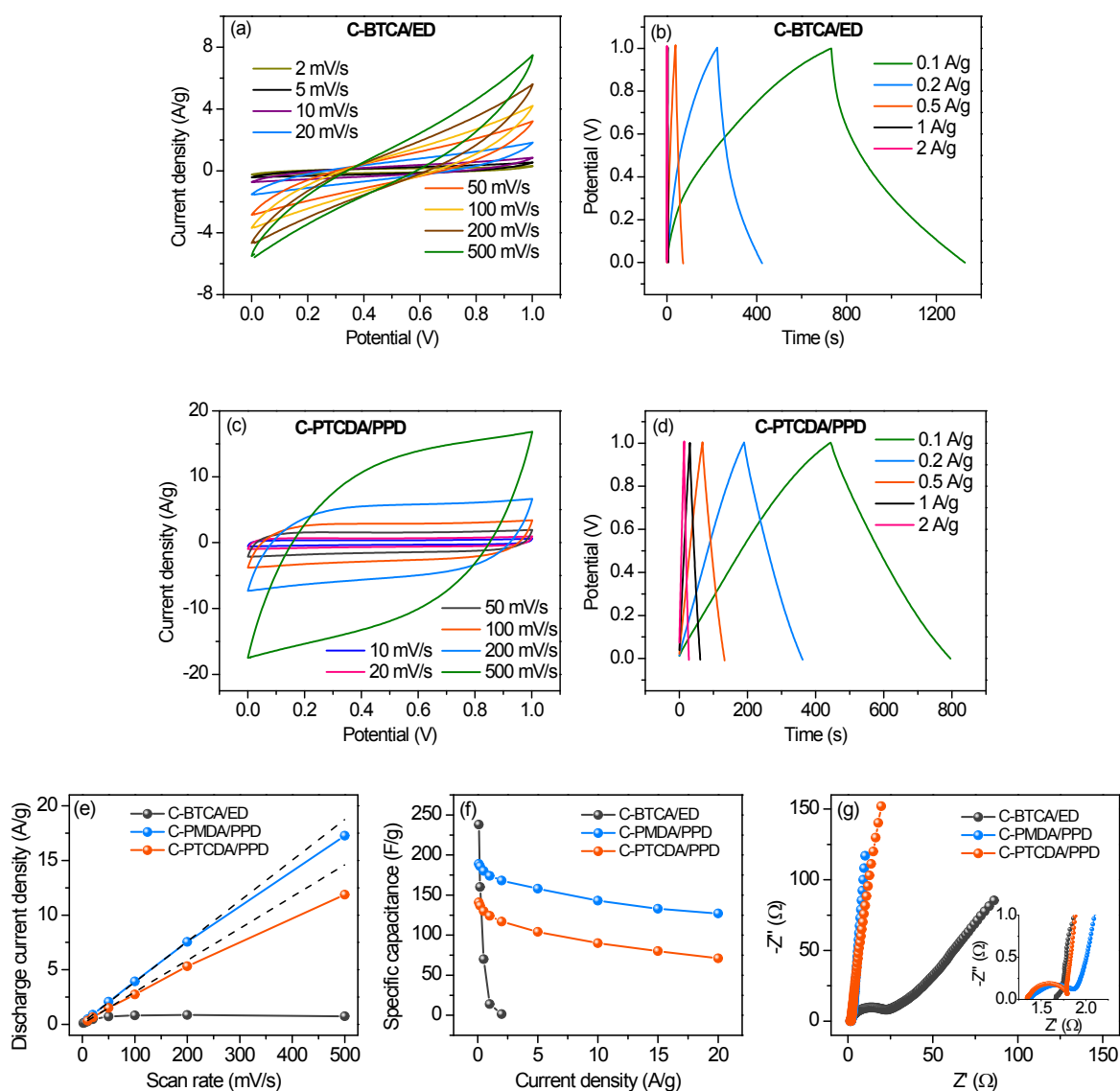
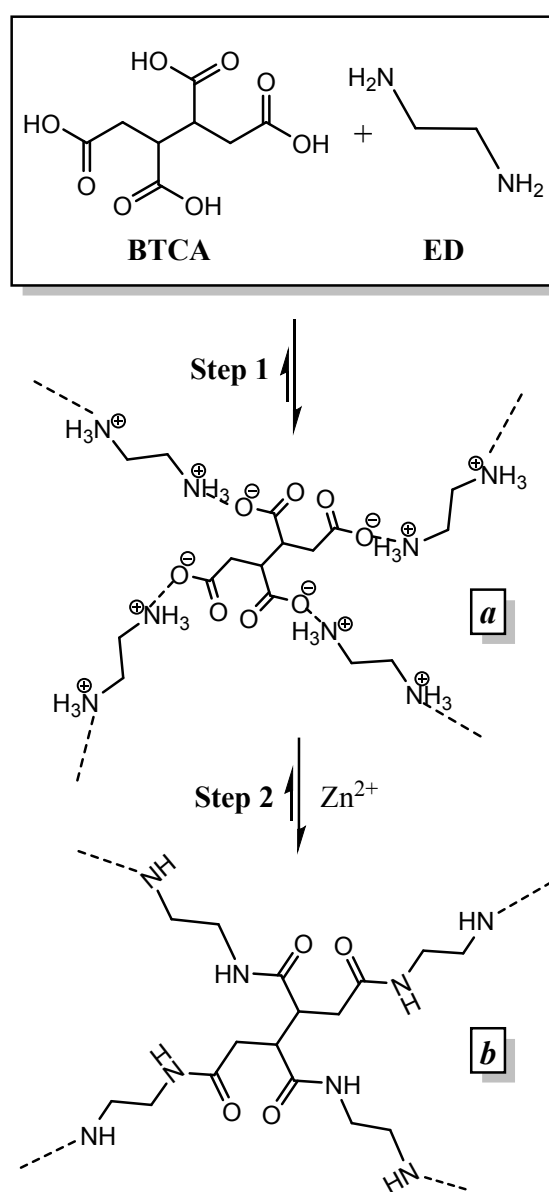


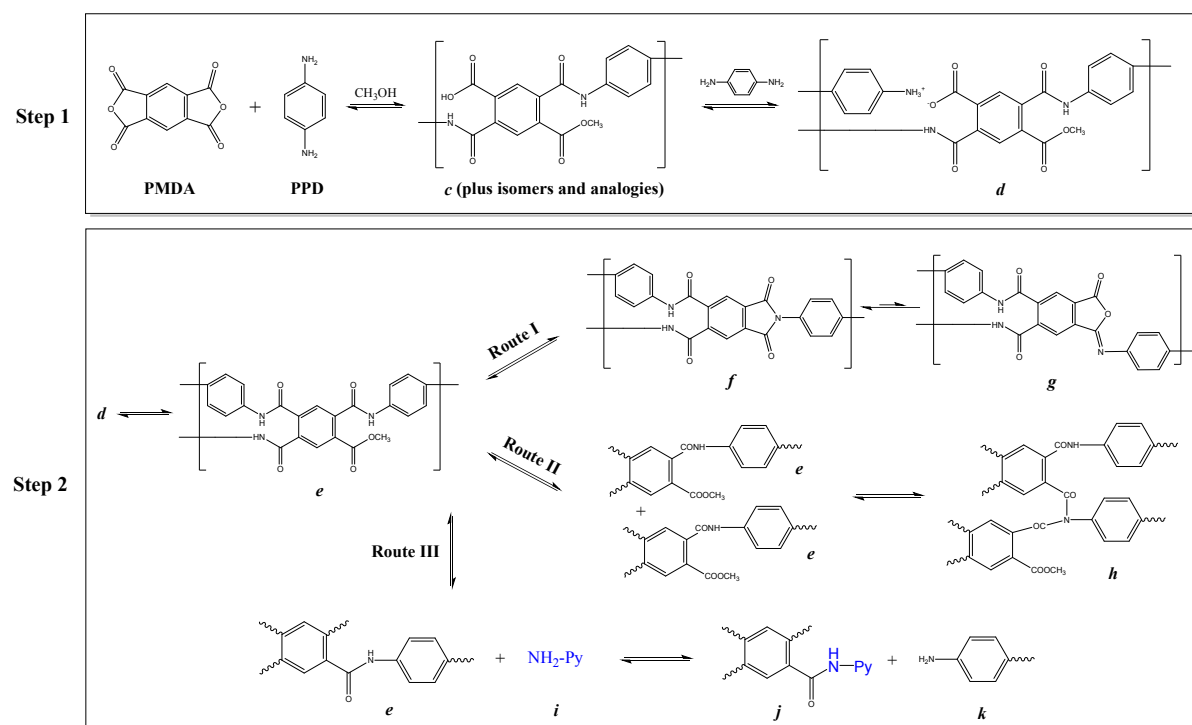
Fig. S1 Electrochemical capacitance results. (a) CV and (b) GCD curves of C-BTCA/ED at different testing rates; (c) CV and (d) GCD curves of C-PTCDA/PPD at different testing rates; and the comparisons of the three carbon electrodes in aspects of (e) evolution of discharge current density versus scan rate at 0.5 V, (f) variation of specific capacitance against current density, and (g) Nyquist plots with insets showing the high frequency regions.

In order to understand the formation mechanism of the porous carbon structures, reaction pathways were proposed here. In the first reaction step between BTCA and ED as illustrated in Scheme S1, an intermediate network structure (*a*) is suggested to be quickly precipitated from methanol solvent at room temperature. The linkages of the network were formed by ion pairs (i.e. salt formation) via proton transfer from BTCA to ED. Since this intermediate structure resembles the zwitterion structure of amino acids which are naturally occurring compounds, this synthetic intermediate is anticipated to be nontoxic, biocompatible and biodegradable. The second reaction step involves the pyrolysis of this intermediate with the presence of uniformly dispersed $\text{Zn}(\text{NO}_3)_2$ salt, in which the cation part (Zn^{2+}) was suggested to be the active centre for catalysis of amidation,⁴ whilst the anion part (NO_3^-) could chemically activate carbon network by forming gaseous species at elevated temperatures. The final carbon structure was based on the robust backbone structure of polyamide (*b*), although the content of heteroatoms would be much eliminated at high carbonization temperatures.⁵ Due to the aliphatic short-chained structure of BTCA and ED, microporous carbon was expected to be the final product of this synthesis approach.



Scheme S1. Proposed reaction mechanism between BTCA and ED in the presence of $\text{Zn}(\text{NO}_3)_2$.

However, the reaction kinetics and mechanisms related to an aromatic dianhydride and an aromatic diamine are clearly very complicated. The schematic reaction pathways of the acid-base pair of PMDA and PPD with the addition of $\text{Fe}(\text{NO}_3)_3$ is shown in Scheme S2. The preparation was also performed in two steps. The first step describes the nucleophilic substitution reaction in methanol solvent by an amine terminal of a PPD molecular at the carbonyl carbon of a PMDA molecular to ring-open the dianhydride structure with the formation of an amide terminal and an ester terminal (**c**) (or carboxylic acid terminal, if water was participated rather than methanol). The excess PPD then treated with the carboxylic acid group to form an ion pair (**d**), similar to the intermediate structure in the BTCA/ED case. This complex polymer network was then pyrolyzed in step-2. At pyrolysis temperatures of $\sim 120\text{ }^\circ\text{C}$, robust amide bonds began to form.⁶ The resulting compound was a mixture of reactive polymer intermediates,⁷ e.g. poly(amide-ester)s (**e**). With increasing temperature, more than three possible reaction routes could be happening simultaneously. Route I was regarded as the most important imidization pathway (**f**) at temperatures in excess of $300\text{ }^\circ\text{C}$.⁶ And it was recognized that the formation of isoimides (**g**) might be more favourable when anhydrides derived from strong acids were used.⁸ However, isoimides isomerize to imide on heating.⁹ Intermolecular link formation was another very important reaction during pyrolysis as shown by Route II in Scheme S2. Adjacent small polymers (**e**) with properly placed reactive sites could condense into larger polymers by forming a thermally stable linkage (**h**), which importantly result in a highly continuous carbon network.¹⁰ Alternatively, amine exchange reaction could also increase the polymer weight as illustrated by Route III. A reactive amine terminal of a smaller polymer backbone (**i**, -Py denotes a polymer backbone) would attack another polymer backbone (**e**) upon the amide linkage, leading to the formation of a higher molecular weight polymer (**j**) and a substituted amine end-group molecule (**k**).¹¹ Besides the reaction pathways discussed above, the real polymer chemistry is far more complicated than we can image. For example, the presence of Fe^{3+} was supposed to coordinate with Lewis bases and catalyse amidation formation,⁴ however, Fe^{3+} might induce free radical species at high temperatures. Moreover, graphitization is yet another complicated process, which could also be catalysed by Fe^{3+} .¹²



Scheme S2. Proposed reaction mechanism between PMDA and PPD in the presence of $\text{Fe}(\text{NO}_3)_3$.

We attempted to validate the above proposed mechanisms by examining the absorbance wavelength of each compound from the UV-vis spectra shown in Fig. S2. A pure chemical was dissolved in a solvent in which a polymer intermediate formed during the sample preparation process. In the preparation of P-BTCA/ED/Zn (Fig. S2a), the two carbon precursors showed an absorbance peak at 205 nm, which correlates to the absorption peak of the polymer intermediate P-BTCA/ED/Zn. Interestingly, the absorption peak of $\text{Zn}(\text{NO}_3)_2$ at 215 nm was greatly reduced in P-BTCA/ED/Zn, implying that $\text{Zn}(\text{NO}_3)_2$ had a strong interaction with the carbon precursor. This phenomenon also occurred in the preparation of P-PMDA/PPD/Fe and P-PTCDA/PPD/Fe (see Figs. S2b and S2c), in which the absorbance peak of $\text{Fe}(\text{NO}_3)_3$ cannot be obviously seen in the polymer intermediate solution. Further work is ongoing to understand the interactions between metal salts and carbon precursors.

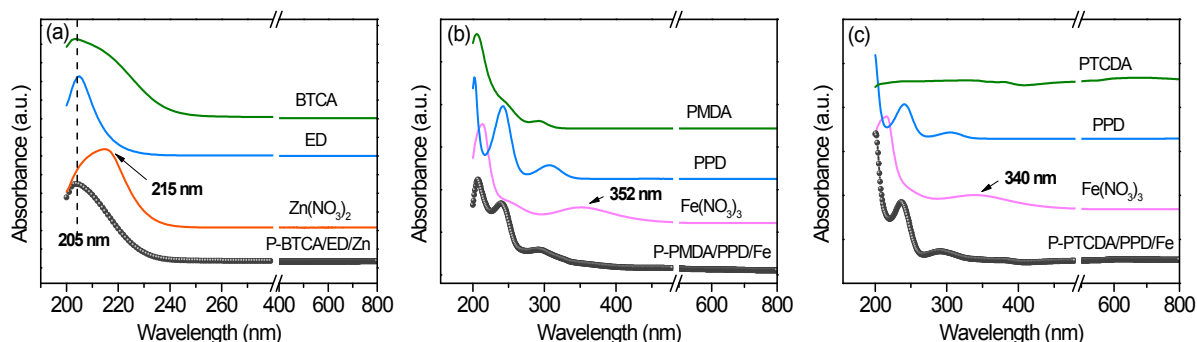


Fig. S2 UV absorption spectra of the precursors and intermediates in the preparations of (a) P-BTCA/ED/Zn, (b) P-PMDA/PPD/Fe, and (c) P-PTCDA/PPD/Fe.

The polymers and carbon products prepared in this work, together with the starting precursors used in the preparations, were characterized by using the FTIR technique. Assignments of the absorption bands were resourced from literature.¹³

Fig. S3a shows the FTIR spectra of BTCA, ED, $\text{Zn}(\text{NO}_3)_2 \cdot 6\text{H}_2\text{O}$, P-BTCA/ED/Zn, and C-BTCA/ED. Pure BTCA exhibited characteristic absorption bands at 3517 cm^{-1} (monomer H-bonded O-H stretch), a broad peak from 3310 to 2340 cm^{-1} (dimer H-bonded O-H stretch), a C=O stretch band at 1695 cm^{-1} , a C-O-H in-plane bend band at 1407 cm^{-1} , and the peak at 1249 cm^{-1} indicated C-O stretching vibration. ED showed a series of $-\text{NH}_2$ stretch bands at 3360 , 3293 and 3192 cm^{-1} , and a pair of $-\text{CH}_2$ stretch bands at 2932 and 2860 cm^{-1} . A band at 1598 cm^{-1} assigned to the deformation of $-\text{NH}_2$. $\text{Zn}(\text{NO}_3)_2 \cdot 6\text{H}_2\text{O}$ showed a strong and broad band at 3350 cm^{-1} assigned to the $-\text{OH}$ absorption from the hydrate shell and absorbed moisture. A set of bands at 1323 , 1047 and 819 cm^{-1} characterizes various vibration modes of the nitrate group. On the other hand, the polymer intermediate P-BTCA/ED/Zn revealed a broad band at 2975 cm^{-1} , indicating $-\text{CH}_2$ vibration modes, and a set of new bands at 1585 cm^{-1} (C-N vibration), 1505 cm^{-1} (N-H deformation) and 1381 cm^{-1} ($-\text{C}-\text{N}-$ stretch). The diminishing of the characteristic C=O stretch (1695 cm^{-1}) of BTCA in the polymer intermediate, the more apparent bands of C-N and N-H, together with the diminishing of the $-\text{OH}$ absorption band indicated chemical interactions among the precursors. It is not surprising to see that the final carbon product C-BTCA/ED had little absorption bands, owing to the substantial loss in heteroatom-functional groups at high pyrolysis temperatures.

Similar phenomena can be seen from Figs. S3b and S3c. The polymer intermediate was not a simple mix of the precursors used in preparing the sample. The observed bands and assignments are listed below.

PMDA (cm^{-1}): 3063 (C-H stretch); 1853 and 1766 (C=O stretching vibration of $\text{O}=\text{C}-\text{O}-\text{C}=\text{O}$); 1508 (stretching of benzene ring skeleton vibration).

PPD (cm^{-1}): 3411 (N-H stretch); 3199 (NH_2 stretch); 3009 (C-H stretch); 1512 (stretching of benzene ring skeleton vibration).

$\text{Fe}(\text{NO}_3)_3 \cdot 9\text{H}_2\text{O}$ (cm^{-1}): 2909 ($-\text{OH}$ stretch); 1322 , 1044 and 815 (vibration modes of the nitrate group).

P-PMDA/PPD/Fe (cm⁻¹): 3000 (-CH stretch); 1724 (-C(O)NH- stretch); 1513 (N-H deformation); 1398 (-C-N-stretch).

PTCDA (cm⁻¹): 3121-3054 (-CH stretch); 1769 (C=O stretching vibration of O=C-O-C=O); 1507 (stretching of benzene ring skeleton vibration).

P-PTCDA/PPD/Fe (cm⁻¹): 3219 and 3057 (-CH stretch); 1771 and 1755 (C=O stretching vibration of O=C-O-C=O); 1593 (stretching of benzene ring skeleton vibration).

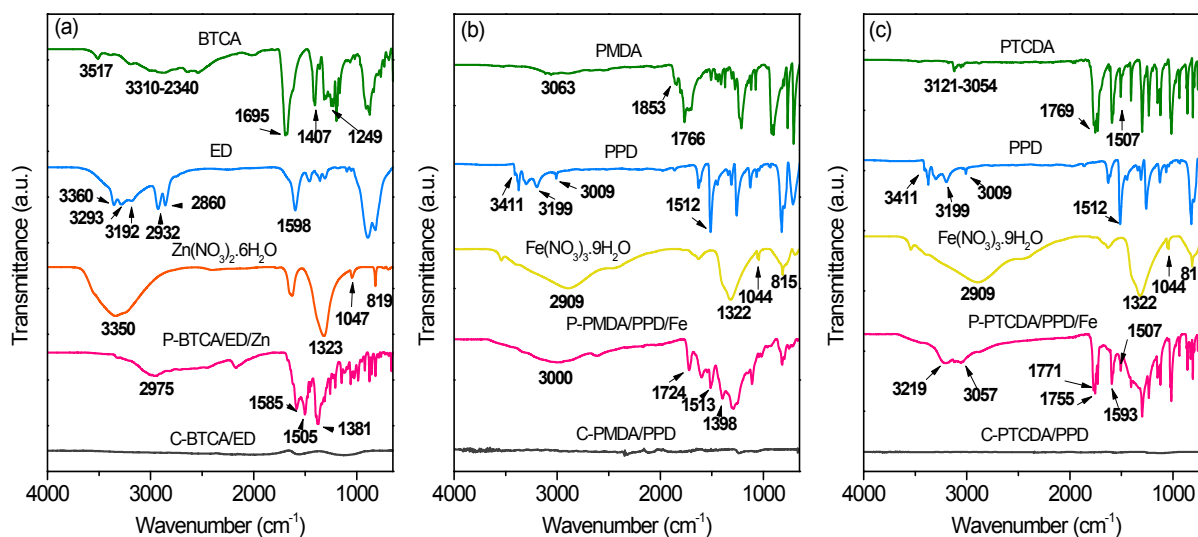


Fig. S3 FTIR spectra of the precursors, intermediates, and final carbon products in the preparations of (a) C-BTCA/ED, (b) C-PMDA/PPD, and (c) C-PTCDA/PPD.

References

1. J. P. Olivier, *Carbon*, 1998, **36**, 1469.
2. M. Kruk, M. Jaroniec and A. Sayari, *Langmuir*, 1997, **13**, 6267.
3. D. Y. Qu and H. Shi, *J Power Sources*, 1998, **74**, 99.
4. Y. Terada, N. Leda, K. Komura and Y. Sugi, *Synthesis-Stuttgart*, 2008, 2318.
5. J. W. Liu, S. Webster and D. L. Carroll, *J Phys Chem B*, 2005, **109**, 15769.
6. C. E. Sroog, *Prog Polym Sci*, 1991, **16**, 561.
7. M. F. Grenierloustalot, F. Joubert and P. Grenier, *J Polym Sci Pol Chem*, 1993, **31**, 3049.
8. J. A. Kreuz, U.S. Pat. 3271366, E.I. du Pont & Co., 1966.
9. R. A. Dinehart and W. W. Wright, *J Appl Polym Sci*, 1967, **11**, 609.
10. R. W. Snyder, B. Thomson, B. Bartges, D. Czerniawski and P. C. Painter, *Macromolecules*, 1989, **22**, 4166.
11. (a) J. B. Tingle and B. F. P. Brenton, *J Am Chem Soc*, 1909, **31**, 1157; (b) M. Hasegawa, Y. Shindo, T. Sugimura, K. Horie, R. Yokota and I. Mita, *J Polym Sci Pol Chem*, 1991, **29**, 1515.
12. (a) F. J. Maldonado-Hodar, C. Moreno-Castilla, J. Rivera-Utrilla, Y. Hanzawa and Y. Yamada, *Langmuir*, 2000, **16**, 4367; (b) W. J. Gao, Y. Wan, Y. Q. Dou and D. Y. Zhao, *Adv Energy Mater*, 2011, **1**, 115; (c) N. P. Wickramaratne, V. S. Perera, B. W. Park, M. Gao, G. W. McGimpsey, S. P. D. Huang and M. Jaroniec, *Chem Mater*, 2013, **25**, 2803.
13. (a) P. Li, Z. P. Xu, M. A. Hampton, D. T. Vu, L. B. Huang, V. Rudolph and A. V. Nguyen, *J Phys Chem C*, 2012, **116**, 10325; (b) Y. Hase, K. Kawai and O. Sala, *J Mol Struct*, 1975, **26**, 297; (c) R. Scholz, M. Friedrich, G. Salvan, T. U. Kampen, D. R. T. Zahn and T. Frauenheim, *J Phys-Condens Mat*, 2003, **15**, S2647; (d) M. G. Giorgini, M. R. Pelletti, G. Paliani and R. S. Cataliotti, *J Raman Spectrosc*, 1983, **14**, 16; (e) Z. H. Liu, H. H. Zhou, Z. Y. Huang, W. Y. Wang, F. Y. Zeng and Y. F. Kuang, *J Mater Chem A*, 2013, **1**, 3454.